IEEE Access
Multidisciplinary ⋮ Rapid Review ⋮ Open Access Journal

Received 3 October 2023, accepted 16 January 2024, date of publication 30 January 2024, date of current version 6 February 2024.

Digital Object Identifier 10.1109/ACCESS.2024.3359696

RESEARCH ARTICLE

Seismic Attribute Extraction and Application Based on the Gabor Wavelet Transform

RAN XIONG[1,3], XURI HUANG[1], LIANG GUO[2], XUAN ZOU[4], AND HAONAN TIAN[5]

[1]State Key Laboratory of Oil and Gas Reservoir Geology and Exploitation, Southwest Petroleum University, Chengdu 610500, China
[2]Department of Railway Engineering, Sichuan College of Architectural Technology, Chengdu 610500, China
[3]Petrochina Hangzhou Research Institute of Geology, Hangzhou 310023, China
[4]Central South Geological Survey Institute of China Metallurgical Geology Burea, Wuhan 430080, China
[5]Petrochina Tarim Oilfield Company, Korla 841000, China

Corresponding author: Liang Guo (hihiwoo@163.com)

This work was supported by the Scientific Research and Technology Development Project of PetroChina Company Ltd. under Grant 2021DJ0501 and Grant 2021DJ1501.

ABSTRACT The most common method for interpreting strata with seismic data is to relate the peaks and troughs of adjacent traces based on the seismic waveform characteristics. This can be captured by machine learning and deep learning methods to stratigraphic segmentation as many people investigated in industry. However, the spatial variability and instability of the peaks and troughs of seismic signals increases the difficulty of applying this technology. In addition, the nonlinear relationship and complicated subsurface geological setting make it more difficult. Thus, we propose a new seismic attribute extraction method based on the Gabor wavelet transform and linear dimensionality reduction. This method does not use the peaks or troughs of the seismic signal and instead focuses on the energy change in the seismic signal at the strata interface. It uses the characteristics of the energy change to identify strata. A sliding window Fourier transforms (STFTs) pretreatment is applied to convert the seismic signal to a spectrum energy form. On this basis, the local texture information of the spectrum can be processed by the Gabor wavelet transform to obtain the Gabor attribute of the seismic signal. The seismic Gabor attributes extracted using the above method contain time, frequency, and energy features, solving the problem of single seismic amplitude data features. Finally, the validity of the extracted seismic attributes is verified by a field data. In this process, the seismic amplitude, spectrum data and Gabor attributes are used as sample data for the support vector machine (SVM), random forest (RF), extreme gradient boosting (XGBoost) models and deep residual shrinkage network (DRSN) for comparison. The results show that when the seismic Gabor attributes are used, the accuracy and root mean square error (RMSE) of the stratigraphic identification with the SVM, RF and XGBoost models are significantly better than those of the seismic amplitude and spectrum data only.

INDEX TERMS Spectrum analysis view, Gabor wavelet transform, LDA, SVM, RF, XGBoost, DRSN.

I. INTRODUCTION

Seismic signals contain various geological information, such as lithology, structure, reservoir petrophysical properties and fluid properties [1], [2]. Early seismic exploration relied on the amplitude or velocity attributes of seismic signals to identify potential oil and gas reservoir reflections by analysing, seismic profiles [3]. The concept of seismic attribute characteristics in seismic exploration work during this period is preliminary. Experts normally process and transform seismic signals to certain forms of data reflecting lithology identification, reservoir description and oil and gas detection [4], [5], [6]. These transformed data can be from wave dynamics, kinematic geometry, statistics and other methods, allowing them to intuitively determine the characteristics of the subsurface geological objects [7], [8], [9]. With the rapid development of mathematics, physics, computer science and information science, various new theories and methods for seismic attribute extraction have been developed [10], [11]. More than hundreds of different seismic attributes based on

The associate editor coordinating the review of this manuscript and approving it for publication was Alberto Cano.

the amplitude, frequency, phase and correlation of seismic signals are available in industry. Still, new seismic attributes and extraction methods are constantly being developed [12].

Seismic attribute extraction can be a mathematical transform process. After seismic data or seismic signals are mathematically transformed, various seismic waves characteristics can be obtained [13]. Seismic signals are non-stationary signals, and studies on the processing of non-stationary signals have began in the 1940s [14]. The short-time Fourier transforms (STFTs) based on stationary signals not being able to handle the non-stationary signals, Koenig et al. proposed a spectrum analysis method [15] to count non-stationary. Because its method is simple and easy to implement, it became a common tool for analysing non-stationary signals and was widely used to analysis and process signals [16], [17], [18]. However, due to lacks of consideration of boundary effect and others, this method was gradually replaced by wavelet transforms, S transforms and Wigner-Ville transforms, which demonstrated superior performance.

In recent years, with the advancement of mathematical theory, computer hardware and technology, various artificial intelligence-based algorithms have been widely used in various fields [19], [20], [21]. In this field, the spectrum analysis has been re-focused. L. Navarro et al. constructed a spectrum analysis) method for music signals to detect subtle frequency and phase changes and successfully characterised each type of sound attack without losing signal information [22]. Yu et al proposed decomposing the mixture spectrogram into three components, namely, a sparse spectrogram representing the singing voice, a low-rank spectrogram representing the background music, and a residual spectrogram representing the components. This successfully separates vocal sounds from background music [23]. Wang et al. treats the time-frequency analysis as an image and further adopts the guided spectrogram filter, and propose a single-channel speech enhancement algorithm. This algorithm effectively suppresses noises and greatly improved speech quality and speech intelligibility [24].

Although studies on the relationship between energy, time and frequency have yielded useful results in speech processing, it is rarely used in seismic signal processing. The frequency spectrum of the seismic signal can be converted into a spectrum analysis to provide a visual representation of the changes in the seismic signal energy with time and frequency. This method is a ''three-dimensional'' form of expression. The process of generating a spectrum analysis view is essentially a process of extracting the seismic signal attributes. Therefore, it is feasible to study and analysis the time-varying characteristics of the short-time spectrum of the seismic signal and extract the relevant attributes of the seismic signal from the energy change. Compared with traditional methods, such as ''bright spot'' technology [25] and ''sweet spot'' [26] technology, the extraction of seismic attributes based on the spectrum analysis view is more objective, accurate and rapid. Furthermore, the seismic attributes extracted from the spectrum analysis view of the effective seismic signal can be used as training data. By applying various machine learning algorithms, seismic signal denoising and pattern recognition can be performed. Gabor wavelet transforms have unique advantages in terms of spectrum analysis view feature extraction. Gabor wavelet transforms can extract features at different scales and various directions in the frequency domain. Compared with the Fourier transform, the Gabor wavelet transform can adjust the direction, centre frequency and fundamental frequency bandwidth of the filter, greatly improving the signal resolution in the time and frequency domains. Tao et al. improved the recognition rate of emotional speech by using Gabor wavelet transforms on the logarithmic energy spectrum of emotional speech [27]. Kubicek et al. developed a feature representation based on the amplitude spectrum of sonar data with convolutions of two-dimensional Gabor wavelet transforms and the acoustic colour amplitude. The Gabor wavelet transform can be used to extract local features for model recognition with high accuracy [28].

Stratigraphic identification is the very important area for seismic interpretation using attributes. Due to the characteristics of wide coverage, spatial continuity and enriched information, seismic data became the major means for constructing stratigraphic framework. Zheng et al. imaged the distribution and evolution of tidal deposits in the study area using RMS (root mean square) amplitude attribute maps by combining high-resolution stratigraphic correlations with seismic attributes extracted from stratigraphic slices of the 3-D data volume [29]. Chen et al. studied on the spatial and temporal distribution of microfacies of the reef-beach using seismic attribute extraction. Meanwhile, combined with impedance inversion, the spatial distribution of porosity of reef-beach reservoir was characterized. The results show that the evolution of the reef-beach system contains three stages which are initial bioclastic bank establishment stage, reef development stage and exposure stage [30]. Thota et al. investigates the reservoir characteristics of the Mount Messenger Formation of Kaimiro-Ngatoro Field which was deposited in deep-water environment. 3D seismic data, core data and well data from the Kaimiro-Ngatoro Field were utilized to identify lithofacies, sedimentary structures, stratigraphic units, depositional environments and to construct 3D geological models [31].

This paper proposes a seismic attribute feature extraction method based on Gabor wavelet transforms of the spectrum analysis view of seismic signals. We first process the seismic signal with framing, windowing, and STFTs to construct the spectrum analysis view. Then, the Gabor wavelet transform is used to extract the time-frequency features, which uses only the seismic waveform features to address the limitation of the traditional method. For experiments, we use the seismic amplitude (waveform), spectrum analysis view and extracted seismic Gabor features as datasets for, three popular machine learning algorithms and one deep learning algorithm, namely,

the support vector machine (SVM), random forest (RF), extreme gradient boosting (XGBoost) and deep residual shrinkage network (DRSN), to verify the effectiveness in terms of the stratigraphic division. The experimental results show that when the seismic Gabor feature is used in the training dataset, the stratigraphic division effect is more noticeable. In addition, we applied the seismic Gabor features to field seismic data and achieved good results.

II. THE PRINCIPLE OF SEISMIC GABOR FEATURE EXTRACTION

A. THE PRINCIPLE OF THE GABOR TRANSFORM

The Fourier transform (FT) is a global transform that may not fit for non-stationary signals. However, non-stationary signals can be considered locally stationary. By performing a FT on the local part of the signal, the characteristics of non-stationary signals can be analysed. In terms of approximation for the stationarity of local signal by Short-Time Fourier Transform (STFTs), we introduce the Gabor transform, which uses the concept of a time window function on the basis of the FT [32]. The Gabor transform performs window processing on the signal, and applies short-time Fourier transforms on the window. By obtaining the transform coefficient, the time-frequency relationship of the signal can be built. Assuming $x(t)$ is a continuous time signal, the continuous Gabor expansion and transform can be defined as,

$$x(t) = \sum_{m}\sum_{n} C(m,n)h_{m,n}(t) \tag{1}$$

$$h_{m,n}(t) = h(t - mT)\exp(jn\Omega t) \tag{2}$$

where T is a time shift parameter, Ω is a frequency parameter, and m and n represent the time domain and frequency domain serial numbers, respectively, with $m, n = 0, \pm1, \pm2, \cdots$. $C(m,n)$ is the Gabor transform coefficient, and $h_{m,n}(t)$ is the Gabor basis function. In addition, the basis function must satisfy the following energy normalization constraint.

$$\int_{-\infty}^{\infty} |h(t)|^2 \, dt = 1 \tag{3}$$

Since the basis function $h_{m,n}(t)$ cannot form an orthonormal basis in the Gabor transform, it is difficult to solve the expansion coefficient $C(m,n)$. Bastiaans proposed a dual window that is biorthogonal to the original window. That is that the biorthogonal analysis window function (auxiliary window function) is used [33]. The Gabor coefficient is calculated by an inner product of the quadrature dual window and the signal [34], that is,

$$C(m,n) = \int_{-\infty}^{\infty} x(t)\gamma^*_{m,n}(t)dt \tag{4}$$

$$\gamma_{m,n}(t) = \gamma(t - mT)\exp(jn\Omega t) \tag{5}$$

where $\gamma^*_{m,n}(t)$ in equation (4) and $\gamma_{m,n}(t)$ in equation (5) are conjugate functions. By substituting equation (4) into equation (1), the following orthogonal relationship can be obtained.

$$\sum_{m}\sum_{n} h_{m,n}(t)\gamma^*_{m,n}(t') = \delta(t - t') \tag{6}$$

where $\delta(t)$ is the Dirac function, which can be expressed as,

$$\delta(t - t') = \begin{cases} 1, & t = t' \\ 0, & t \neq t' \end{cases} \tag{7}$$

The biorthogonal condition can be expressed as,

$$\frac{T_0\Omega_0}{2\pi}\int_{-\infty}^{\infty} h(t)\gamma^*(t - mT_0)\exp(-jn\Omega_0 t)dt = \delta(m)\delta(n) \tag{8}$$

where $T_0 = 2\pi/\Omega$, and $\Omega_0 = 2\pi/T$.

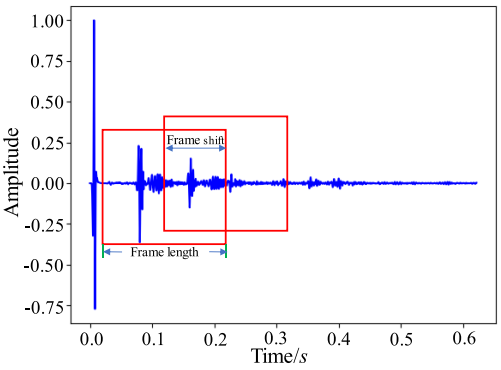

FIGURE 1. Schematic diagram of seismic time-domain signal framing.

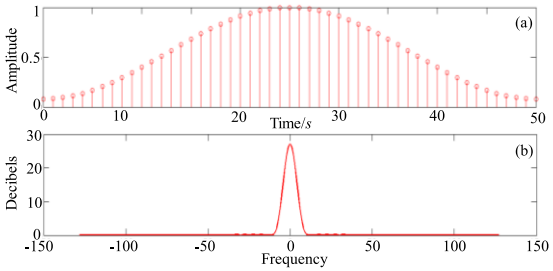

FIGURE 2. Schematic diagram of the Hamming window function. (a) is the time-domain image, and (b) is the frequency domain image.

B. SPECTRUM ANALYSIS VIEW OF SEISMIC SIGNALS

In this paper, we use the short-time window analysis to process the seismic signal and to divide the signal into multiple short segments, assuming the signal to be stationary in the short segments [35]. The segmentation of the seismic signal results in possible segment discontinuity at its split point in between segments. The more the segments are divided, the higher the error between the divided signal and the original signal. Therefore, we perform windowing or framing on the segmented signal.

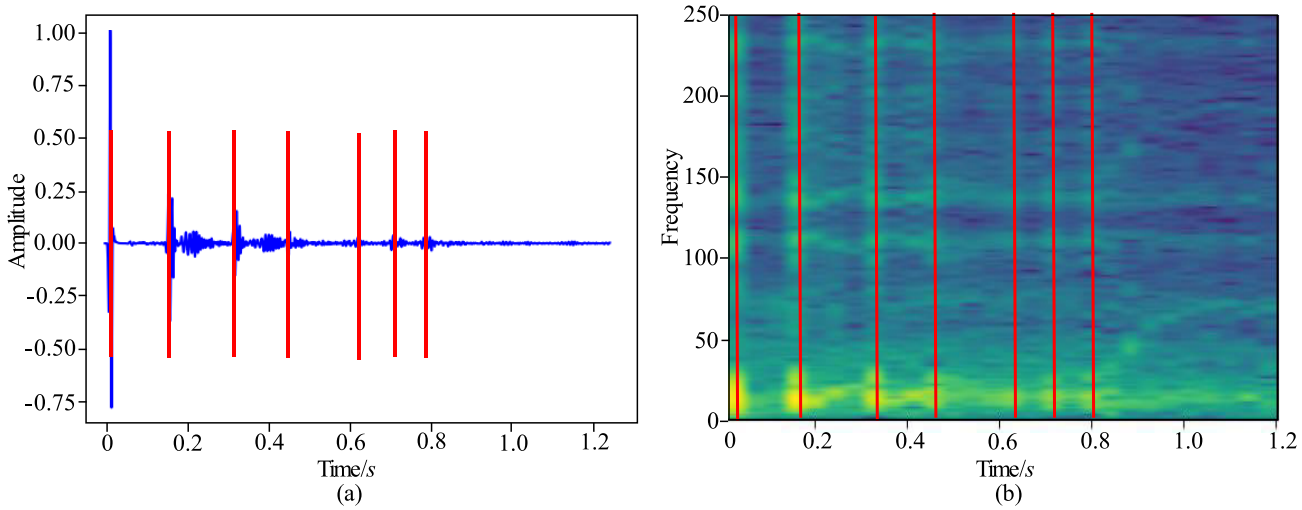

FIGURE 3. Spectrum analysis view of seismic single-track data. (a) Raw seismic signal amplitude, (b) Spectrum analysis view of the seismic signal. The red line is the stratigraphic boundary.

1) SEISMIC SIGNAL FRAME PROCESSING

If the seismic signal is processed in frames, the signal can be considered a stationary signal in each frame. Then, STFT processing can be performed. To maintain the continuity of the signal, a segmented method in which the front and rear of each frame are partially overlapped is used to smooth the transition between frames or segments. The overlapping part is the frame shift, as shown in Fig. 1.

2) SEISMIC SIGNAL WINDOWING

Windowing the seismic signal is equivalent to periodically extending a truncated signal. Thus, the truncated signal becomes a finite sequence. Because this operation causes the original nonperiodic signal to reflect some of the characteristics of the periodic function, the time-domain signal can better meet the periodic requirements of STFT. In addition, the framed seismic signal becomes continuous after windowing, which suppresses spectral leakage and aliasing and prevents the Gibbs effect. The windowing process is usually realized by multiplying the signal and the window function. The equation (9) and equation (10) show the windowing process in the time and frequency domains.

$$x_w(n) = x(n)w(n) \tag{9}$$

$$X_N\left[\exp(j\omega)\right] = 0.5\int_{-\pi}^{\pi} X\left[\exp(j\theta)\right] \times W\left[\exp(j(\omega-\theta))\right]d\theta \tag{10}$$

In this paper, the window function is the Hamming window, which is defined as,

$$w(t) = \begin{cases} \frac{1}{T}(0.54 + 0.4\cos\frac{\pi t}{T}) & |t| \le T \\ 0 & |t| > T \end{cases} \tag{11}$$

$$W(\omega) = 1.08\frac{\sin\omega T}{\omega T} + 0.46\left[\frac{\sin(\omega T+\pi)}{\omega T+\pi} + \frac{\sin(\omega T-\pi)}{\omega T-\pi}\right] \tag{12}$$

Different weighting coefficients in the Hamming window decrease the size of the side lobes and cause the energy of the signal to be more concentrated. The Hamming window is more suitable for seismic signals with complex spectra and multiple frequency components, as shown in Fig. 2.

3) SPECTRUM ANALYSIS VIEW OF SEISMIC SIGNALS

After the seismic signal $x(t)$ is divided into frames and windowed, the seismic signal sequence $x_d(n)$ is obtained with $d = (1, 2, \cdots, D)$, where D represents the number of frames. The seismic signal of the third frame is calculated. The equation for calculating the STFT of the seismic signal $x_d(n)$ of the *d-th* frame is:

$$X_d(k) = \sum_{n=0}^{N-1} x_d(n)w(n_0-n)\exp\left[-(2\pi j/N)kn\right] \tag{13}$$

where $w(n_0-n)\exp\left[-(2\pi j/N)\,kn\right]$ is the discretized Hamming window function, N is the interval length of the short-time Fourier transform, and $X_d(k)$ is the spectrum analysis view of the generated seismic signal. The seismic signal spectrum analysis view contains a considerable amount of information related to the seismic attribute characteristics. This view combines the characteristics of the time-domain waveform and spectrogram and shows the variation relationship of the seismic signal spectrum over time, which is a dynamic expression of the spectrum.

Fig. 3 shows a spectrum analysis view of a single trace seismic signal generated from multi-reflecting interface or strata boundaries. In the spectrum analysis view, the horizontal axis is time, the vertical axis is frequency, and the the

colour is the energy at a specific time and frequency, as shown in Fig. 3(b). When the spectrum analysis view is studied along the time axis, we find that the energy is mainly concentrated in the low frequency band and is not continuous. The energy concentrated area (usually the resonance peak) is mainly near the reflective layer. The energy gradually decays over time. When the spectrum analysis view is studied along the frequency axis, we find that the early energy is concentrated in the high frequency band near the reflection horizon. However, this energy is much lower and attenuates faster than in the low frequency band. This result is consistent with the propagation characteristics of seismic waves in the strata. Therefore, compared to the direct extraction of seismic attribute from seismic signal waveforms, the seismic signal spectrum analysis view can more objectively reflect the propagation characteristics of seismic signals in subsurface media.

C. GABOR WAVELET TRANSFORM AND FEATURE EXTRACTION IN THE SPECTRAL ANALYSIS VIEW

1) GABOR WAVELET TRANSFORM

The Gabor function is orthogonalized through scaling and rotations for a series of Gabor wavelets. A Gabor wavelet has a high resolution in both the time and space domains. In addition, the Gabor wavelet is able to capture local features and can be used to extract subtle local changes in data. The two-dimensional Gabor wavelet kernel function can be expressed as,

$$G_{\mu,v}(z) = \frac{\|k_{\mu,v}\|}{\sigma^2} \exp\left(-\frac{(-\|k_{\mu,v}\|^2\|z\|^2)}{2\sigma^2}\right) \times \left[\exp\left(jk_{\mu,v}z\right) - \exp\left(-\frac{\sigma^2}{2}\right)\right] \quad (14)$$

where $k_{\mu,v} = \begin{pmatrix} k_v \cos\varphi_\mu \\ k_v \sin\varphi_\mu \end{pmatrix}$, $k_v = 2^{\wedge}\left(-\frac{v+2}{\pi}\right)$, $\varphi_\mu = \mu\frac{\pi}{k}$, μ is the direction of the Gabor filter, v is the filter scale, k is the total number of directions, j is the complex arithmetic ($j = \sqrt{-1}$), σ is the radius of the Gaussian function, $\|\bullet\|$ is the Euclidean norm of the corresponding value, and $z(x, y)$ is the spatial position of the input value. The single-channel seismic signal data can be converted to the spectrum analysis view and recorded as $P(z)$. The convolution of the Gabor wavelet can be expressed as follows:

$$F_{u,v}(z) = P(z) * G_{\mu,v}(z) \quad (15)$$

where $F_{u,v}(z)$ is the feature of the spectrum analysis view $P(z)$ with the Gabor wavelet transform, and $*$ is the convolution operation.

2) SEISMIC GABOR FEATURE EXTRACTION

The size of the kernel function window in the Gabor wavelet transform has a great influence on the feature extraction of the seismic spectrum analysis view. In equation 13, the kernel function window size can be adjusted according to the (x, y). We fix the relevant parameters of the different scales and directions to qualitatively analyse the influence of the kernel function window size on feature extraction. The specific parameters include λ which is the wavelength, θ which is the filter direction, φ which is the phase offset, being able to represent the phase parameter in the cosine function in the Gabor kernel function, and γ which is the spatial aspect ratio, indicating the ellipticity of the Gabor kernel function. When γ is equal to 1, the filter is circular. When γ is greater than 4 or less than 1, the filter is either elongated or shortened, respectively. The changes as the direction of the Gabor filter varies can be observed by selecting different window sizes, as shown in figures 4 and 5.

As seen in figures 4 and 5, as the window size of the kernel function increases, the non-zero proportion of the convolution kernel decreases, and the features extracted by this filter gradually capture more details. Due to seismic data denoising in the early stage, it is impossible to completely eliminate the interference factors. The features extracted by the large window amplify the interference factors and are sensitive to interference such as noise. The extracted features are more likely to contain interference factors. In addition, as the window size increases, the computation demand increases. However, the features extracted by a small window tend to be global, which can miss the detailed features and reduce the resolution of the extracted features. Therefore, it is necessary to select the optimal window size through experiments.

D. THE BASIC PROCESS OF DIMENSIONALITY REDUCTION

Linear discriminant analysis (LDA) is a dimensionality reduction technique for data analysis and supervised learning. The idea of LDA is that when projecting variables, the variance in the inner class has the smallest value, while the variance between classes has the largest value [36], [37]. For stratigraphic boundary identification, the projection points corresponding to a boundary being as close as possible, which the distance between different types of data centre points to be as large as possible. The specific process is as follows.

1) Consider 7 hierarchical interfaces of data $\{x_i, y_i\}_{i=1}^{7}$, where the data of $\{x_i, y_i\}$ is the *i-th* interface, with $i \in [1, 2, \cdots, 6, 7]$.

2) Calculate the covariance matrix $\sum_i$ of the i-th layer.

3) Calculate the projections $\omega^{\mathrm{T}}\mu_0$ and $\omega^{\mathrm{T}}\mu_1$ of the hierarchical interface data on line w, where μ_0 and μ_1 indicate the position of the line point in the data.

4) Calculate the covariances $\omega^{\mathrm{T}}\sum_0\omega$ and $\omega^{\mathrm{T}}\sum_1\omega$ of the two hierarchical interfaces separately.

5) According to the principle that the projection points of the same interface should be as close as possible, that is, $\omega^{\mathrm{T}}\sum_0\omega + \omega^{\mathrm{T}}\sum_1\omega$ should be as small as possible.

6) Perform projection points of different interfaces to have group center distance as large as possible, that is, $\|\omega^{\mathrm{T}}\mu_0 - \omega^{\mathrm{T}}\mu_1\|_2^2$ should be as large as possible.

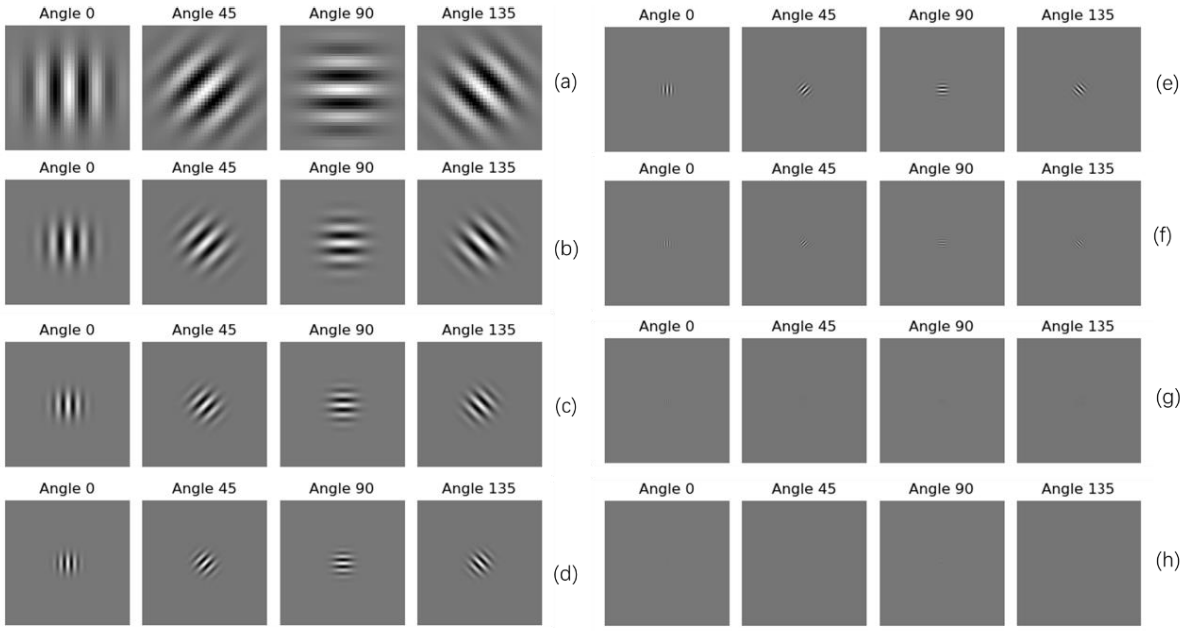

FIGURE 4. The shape changes in the Gabor kernel filter with different scales and directions.

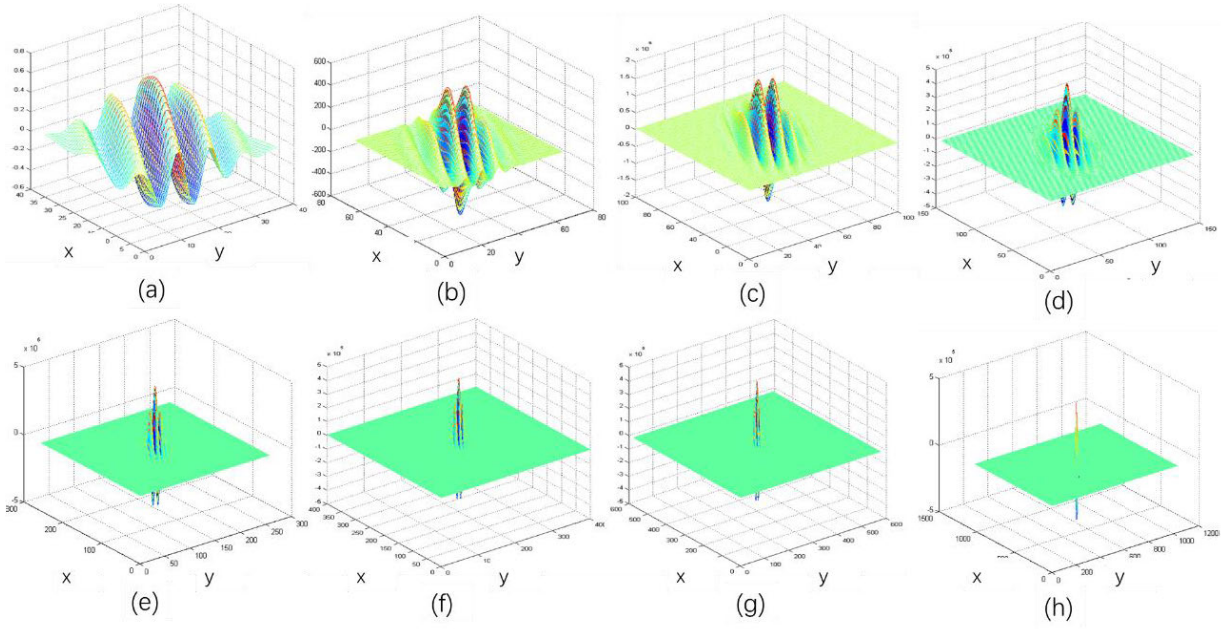

FIGURE 5. Gabor kernel filter shape changes with different window sizes. (a) 6 × 6, (b) 8 × 8, (c) 10 × 10, (d) 12 × 12, (e) 16 × 16, (f) 20 × 20, (g) 24 × 24, and (h) 32 × 32.

7) Maximize objective function J as equation (16) as follows.

$$J = \frac{\left\|\omega^{\mathrm{T}}\mu_0 - \omega^{\mathrm{T}}\mu_1\right\|_2^2}{\omega^{\mathrm{T}}\sum_0 \omega + \omega^{\mathrm{T}}\sum_1 \omega} \tag{16}$$

equation (16) can be rewritten as,

$$J = \frac{\omega^{\mathrm{T}}(\mu_0 - \mu_1)(\mu_0 - \mu_1)^{\mathrm{T}}\omega}{\omega^{\mathrm{T}}(\sum_0 + \sum_1)\omega} \tag{17}$$

According to the form of generalized Rayleigh Quotient, equation (17) can be reformulated as,

$$J = \frac{\omega^{\mathrm{T}} S_a \omega}{\omega^{\mathrm{T}} S_b \omega} \tag{18}$$

where S_a and S_b are the intraclass scatter matrix and interclass scatter matrix, respectively.

To optimize equation (18), the following equation can be derived.

$$\omega^* = \arg\max_{\omega} \frac{\left|\omega^{\mathrm{T}} S_a \omega\right|}{\left|\omega^{\mathrm{T}} S_b \omega\right|} \tag{19}$$

where ω^* is the optimal discriminant function. In order to achieve the goal, we differentiate equation (18).

$$\frac{dJ_{(\omega)}}{d\omega} = \frac{2S_a\omega\left(\omega^{\mathrm{T}} S_b \omega\right) - 2S_b\omega\left(\omega^{\mathrm{T}} S_a \omega\right)}{\omega^{\mathrm{T}} S_b \omega} \tag{20}$$

We set equation (20) equal to 0, and we can get the following equation.

$$S_a\omega\left(\omega^{\mathrm{T}} S_b \omega\right) = S_b\omega\left(\omega^{\mathrm{T}} S_a \omega\right) \tag{21}$$

Equation (21) can be transformed into the following equation.

$$S_a\omega = S_b\omega\left(\frac{\omega^{\mathrm{T}} S_a \omega}{\omega^{\mathrm{T}} S_b \omega}\right) = J(\omega) S_b \omega \tag{22}$$

We multiply both sides of equation (22) by S_b^{-1} to get the following equation.

$$S_b^{-1} S_a \omega = J(\omega)\omega \tag{23}$$

where, S_b^{-1} represents the inverse matrix of S_b. So solving ω^* is to solve the eigenvectors and eigenvalues corresponding to $S_b^{-1} S_a$. Derived from the above equation, LDA is divided into three steps. The first is to obtain classification information, and secondly to obtain the average value, within-class scatter matrix, and between-class scatter matrix. Finally, find the eigenvalue corresponding to $S_b^{-1} S_a$.

E. SPECTRUM ANALYSIS VIEW OF SEISMIC SIGNALS

The spectrum analysis process has two components including data processing and feature extraction. The former is responsible for generating the spectrum analysis view, while the latter extracts the features of the spectrum analysis view. The purpose of this study is to address a limitation of the traditional method, which uses extracting only the seismic attribute features of the waveform features. First, each sample of the data is intercepted with window when sliding. To address the data interception issue caused by the nonuniform thickness of the strata while effectively extracting thin layer features, the method of minimum window overlapping and moving is adopted. The minimum window is chosen based on the premise of having no more than the number of data points corresponding to window of the thinnest layer in the entire section.

Due to the large amount of seismic data, the selected window must consider thin layers and not be too large. In addition, overlapping motion inevitably leads to duplicate calculations, thereby reducing efficiency. Therefore, for different thicknesses of strata, different data interception methods are used. For strata with large thicknesses, the window is moved from the top to the bottom by connecting the end of the window. When the data near the bottom are smaller than the length of the window, the method of superimposing and moving is used to prevent the loss of the bottom data. For data interception at the stratigraphic interface, the window size is based on parameters such as the wavelength and sample rate. We attempt to prevent the window being too large, as the data could intercept the horizon data, causing the data to be corrupted. We also attempt to prevent the window beingtoo small, which could cause reflection data to be missed. The specific process is shown in Fig. 6.

III. MODEL TRAINING AND PARAMETER SETTING

A. DATA PREPARATION AND EVALUATION INDEX

200 samples seismic profile data were selected as the dataset for an experiment, with 180 samples in the training set and 20 samples in the test set. Each seismic section has a total of 7 stratigraphic boundaries, as shown in Fig. 7.

A seismic profile consists of the amplitude data. The distribution interval of the seismic amplitude data in the same study area is particularly large. The seismic data should be standardised to increase the ease of determining the optimal solution after the distribution interval reaches $[-1, 1]$, accelerating the convergence of the model. Furthermore, in this experiment, the resulting data which additional gain is applied from processing are used instead of the original waveform data. To mitigate the uncertainty caused by this gain, the data were normalized. To improve the computational efficiency, we normalized the amplitude data. The serial numbers 1 through 7 were used as stratigraphic labels for the 7 interfaces, with 0 used to represent the remainder of the stratigraphic data. It should be noted that when the training set for the model is created, the division of the strata uses the trough of the seismic wave as the starting point. Therefore, the division points of the strata all fall in the trough of the seismic wave.

The evaluation criteria are the root mean square error (RMSE) and accuracy. The RMSE is calculated as follows.

$$RMSE = \left[\sum_{i=1}^{7}\sum_{j=1}^{400}(\hat{y}_{ij} - y_{ij})/2800\right]^{1/2} \tag{24}$$

where i and j are the serial number and track number of the layered interface, respectively, $\hat{y}_{ij}$ is the position of the predicted interface point, and y_{ij} is the position of the true interface point. The RMSE considers only the degree of difference between the predicted stratigraphic interface and the true stratigraphic interface and is easily affected by extreme values. On the basis of RMSE, we also use the accuracy rate as an evaluation metric. In the artificial stratigraphic division, a certain range of errors are allowed. Thus, we simulate stratigraphic division with a threshold control. Specifically, when the threshold value is 1, the predicted interface completely coincides with the true interface, and the stratigraphic division is correct. When the threshold is 2, the predicted interface points and the true interface point has one sample difference in either direction. When the threshold is 3, the

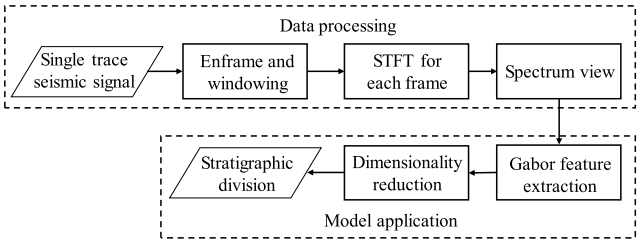

FIGURE 6. Flowchart of this paper. The main steps and processes in the figure are as follows: 1. Framing and windowing the seismic signal data, 2. Short-time Fourier transform of each frame of the seismic signal data, 3. Generating a spectrum analysis view of the seismic signal, 4. Gabor filtering, in which the frequency spectrum analysis view is processed to obtain the relevant eigenvalues at different scales and directions, 5. Use LDA to obtain the optimal feature dimension, and 6. Stratigraphic division to verify the extracted features.

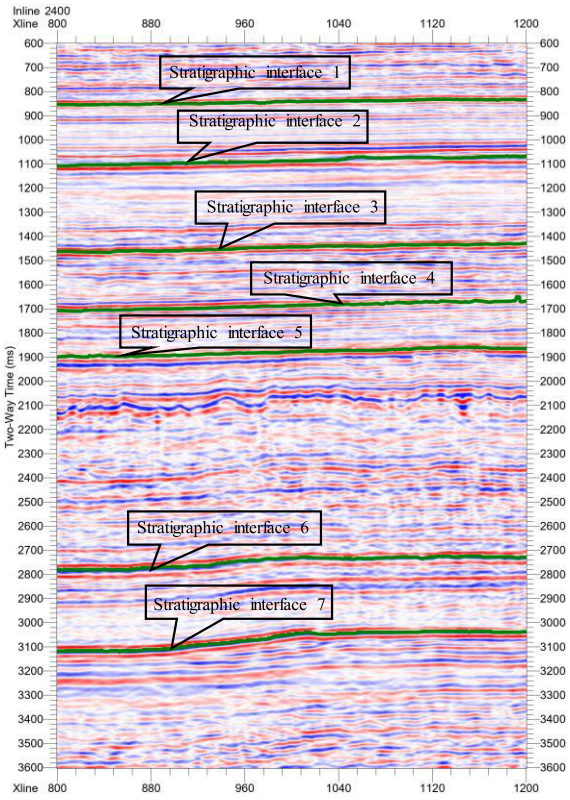

FIGURE 7. Stratigraphic division of the seismic profile. Taking the 2400 profile as an example, each seismic profile consists of 401 single traces. Serial numbers from 800 to 1200 make up the abscissa. The ordinate is time (which can be regarded as depth), and the sampling time of each single-channel data is 3600 *ms*. To reduce the calculation cost, we intercept the data in the time period from 600 *ms* to 3600 *ms*. The sampling interval is 2 *ms*.

predicted interface point and the true interface point have 2 sample difference in either direction, and so on.

B. CHOICE OF TEMPLATE SIZE

To demonstrate the validity of the Gabor feature of the seismic data, we tested the template size for feature extraction. The Gabor features extracted with different template sizes have various enhancement. A Gabor feature with a scale of 17 and an orientation of 150° is shown in Fig. 8.

Before the Gabor template size is designed, it should be noted that the window size of the time domain and the template size of the Gabor kernel function is different. The time domain window size is inversely proportional to the centre frequency and can be calculated as follows.

$$L = \frac{\sqrt{2}\pi}{\omega} \tag{25}$$

where L is the time domain window size, and ω is the centre frequency.

We conduct experiments with SVM, RF, XGBoost and DRSN classifiers using convolutions with template sizes of 8×8, 16×16 and 32×32. The experimental results are shown in Table 1.

Table 1 shows that the 32×32 template achieves the best layering effect. The RMSEs of the SVM, RF, XGBoost and DRSN classifiers are 0.120, 0.139, 0.115, and 0.123 respectively. For the SVM classifier, the RMSEs of the 32×32 template is 0.157 and 0.036 less than those of the 8×8 and 16×16 templates. For the RF classifier, the RMSEs of the 32×32 template is 0.168 and 0.026 less than those of the 8×8 and 16×16 templates. For the XGBoost classifier, the RMSEs of the 32×32 template is 0.136 and 0.037 less than those of the 8×8 and 16×16 templates. For the DRSN classifier, the RMSEs of the 32×32 template is 0.09 and 0.025 less than those of the 8×8 and 16×16 templates. In terms of computing time, the SVM, RF, XGBoost and DRSN classifiers took 9.43, 10.04, 9.13 and 10.05 *hours*, respectively, with the 32×32 template. The classifiers took 7.06 *hours*, 8.75 *hours*, 7.84 *hours* and 8.94 *hours* for the 16×16 template and 5.78, 6.98, 6.04 and 7.68 *hours* for the 8×8 template. Considering both performance and efficiency, we chose a template size of 16×16 for subsequent experiments.

C. FEATURE DIMENSIONALITY REDUCTION

The experiments in this section use LDA to reduce the dimensionality of the seismic Gabor features. The SVM, RF, XGBoost and DRSN classifier were adopted. The test data included 20 seismic profiles. The results are shown in Fig. 9.

Fig. 9(a) shows that as the dimension increases to 25000, the accuracies of the three classifiers improve. As the dimension increases further, the performance of the classifiers decreases. The number of dimensions corresponding to the best performance of each classifier is that the SVM has the highest accuracy for the dimension of 24000, while 2400 and 2500 for the RF classifier 2500 for XGBoost and 2100 for DRSN classifier. When the dimensionality is reduced further, the accuracies of the three classifiers decrease. In addition, Fig. 9(b) shows the time consumption of each classifier for different feature dimensions. As the dimension increases, the individual classifiers take longer to train the model. According to the model training time and the stratification accuracy we chose an average dimension of 24000 for the subsequent experiments, at which the three classifiers achieved the best performance. Finally, we compare the results with the Gabor

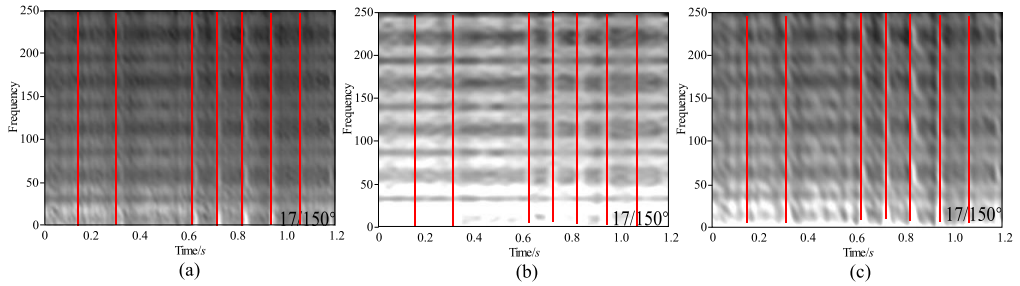

FIGURE 8. Gabor characteristics of seismic single-trace data with different template sizes. The red lines are the stratified points on the seismic single-track data. The scale in the figure is 17 and the direction is 150°. (a) is a Gabor feature with a template size of 8 × 8. (b) is a Gabor feature with a template size of 16 × 16. (c) is a Gabor feature with a template size of 32 × 32. As the size of Gabor kernel function template increases, the details of single-channel seismic spectrum analysis view feature extraction gradually improve.

TABLE 1. Accuracy and time of different template sizes.

Template Size	SVM		RF		XGBOOST		DRSN	
	RMSE	Time (*h*)	RMSE	Time (*h*)	RMSE	Time (*h*)	RMSE	Time (*h*)
8×8	0.277	5.78	0.307	6.98	0.251	6.04	0.213	7.68
16×16	0.156	7.06	0.165	8.75	0.152	7.84	0.148	8.94
32×32	0.120	9.43	0.139	10.04	0.115	9.13	0.123	10.05

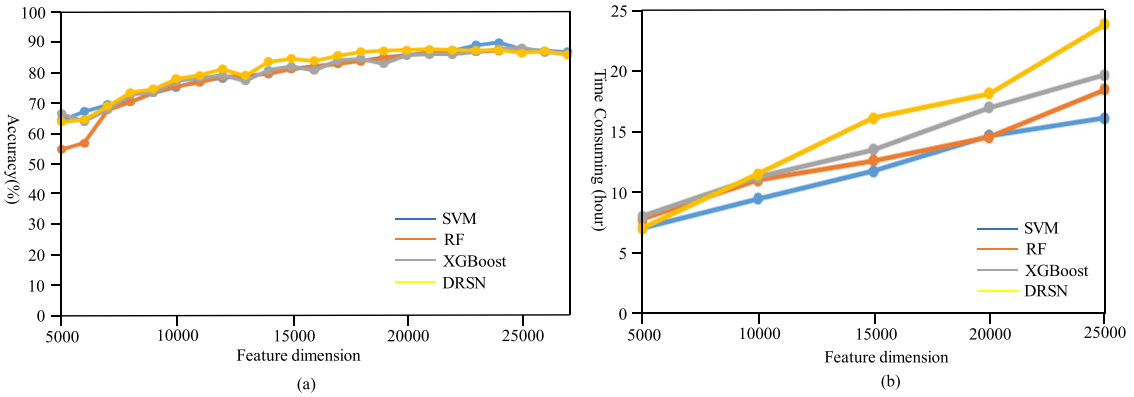

FIGURE 9. Stratigraphic division effect and model training efficiency of different feature dimensions. (a) is the accuracy rate, and (b) is the time consumption.

feature without LDA dimensionality reduction. The comparison results are shown in Table 2. Table 2 shows that the performance of each classifier is greatly improved by LDA dimensionality reduction. In addition, the time consumption is greatly reduced. The experiments show that when LDA is used to reduce the dimension, the Gabor feature can also preserve critical striatal characteristics. LDA greatly reduces the computational complexity of the classifier.

TABLE 2. Comparison of the effect and time before and after dimensionality reduction (threshold: 3).

Classifier	Before Dimensionality Reduction			After Dimensionality Reduction		
	RMSE	Accuracy (%)	Time (*h*)	RMSE	Accuracy (%)	Time (*h*)
SVM	0.156	89.21	7.06	0.126	92.93	5.35
RF	0.165	86.03	8.75	0.129	90.02	5.91
XGBoost	0.152	85.91	7.84	0.125	90.68	5.82
DRSN	0.148	90.21	8.94	0.117	90.33	6.05

IV. ANALYSIS AND APPLICATION

A. EXPERIMENTAL RESULTS AND ANALYSIS

To verify the validity of the Gabor feature of the seismic data, we use the seismic amplitude data, spectrum analysis view data and Gabor features as training set. The stratigraphic division experiments are conducted using the SVM, RF, XGBoost and DRSN classifiers. The experimental results are shown in Table 3.

For comparison purpose, the threshold was set to 3 to analysis the experimental results. The classifiers trained with the seismic amplitude data as the training set had the poorest RMSE and accuracy. The classifiers trained with addition of the spectral analysis view features achieves better RMSE and accuracy. With addition of Gabor feature is the best. For the SVM classifier, the RMSE is 0.257, and the accuracy was

TABLE 3. Stratigraphic division effect of different features at different thresholds.

Type of Data	RMSE				Threshold	Accuracy (%)			
	SVM	RF	XGBoost	DRSN		SVM	RF	XGBoost	DRSN
Seismic Amplitude Data	0.257	0.264	0.260	0.215	1	50.21	48.81	49.54	50.14
					2	66.84	62.54	65.79	67.24
					3	68.41	78.06	76.52	79.15
					4	72.52	80.32	78.90	84.15
					5	81.46	82.89	80.11	87.43
Spectrum Analysis View	0.216	0.201	0.203	0.207	1	54.01	58.14	56.10	58.54
					2	65.58	68.86	67.73	70.25
					3	71.00	72.45	79.64	80.33
					4	79.13	78.09	80.32	87.45
					5	86.75	88.26	85.12	90.68
Seismic Gabor Characteristics	0.126	0.129	0.125	0.117	1	54.82	52.29	61.42	65.14
					2	74.42	80.54	76.55	82.04
					3	92.93	90.02	90.68	90.33
					4	94.97	94.71	94.66	95.38
					5	95.04	95.36	95.82	97.41

68.41%. With addition of spectral analysis view data had an RMSE of 0.216 and an accuracy of 71%. The RMSE with further addition of the seismic Gabor feature is 0.126, and the accuracy was 92.93%. Compared with addition of the seismic amplitude data and the spectral analysis view features in the training sets, the RMSE of the seismic Gabor features is decreased by 0.131 and 0.09, respectively, while the accuracy increased by 24.52% and 21.93%.

With the RF classifier, compared with the seismic amplitude data and the spectral analysis view features, the RMSE of the seismic Gabor features decreased by 0.135 and 0.066, respectively, while the accuracy increased by 11.96% and 17.57%. With the XGBoost classifier, compared with the seismic amplitude data and the spectral analysis view features, the RMSE of the seismic Gabor features decreased by 0.135 and 0.078, respectively, while the accuracy increased by 14.16% and 11.04%. In terms of the RMSE and accuracy, horizon division with the Gabor features as the dataset achieved the best results, as shown in Fig. 10.

An analysis of 20 tests shows that training datasets with various attributes have different impacts on the performance of the classifier, while the stratigraphic division performance of different classifiers on the same dataset is not considerably different.

To further analyse the specific impact of the three datasets on the performance of the classifier, a single channel of the SVM classifier was extracted, and the specific results of the stratification are shown in Fig. 11.

When the seismic amplitude data are used as the training set, the stratigraphic division result is imprecise, as shown in Fig. 11(a). The division of the first stratigraphic interface deviates dramatically from that of the original interface. The considerable differences can be observed. In the subsequent division, the interface points are mis-labelled. For the entire trace, only the fifth layer is correct. The overall fitting is poor. For the training set with addition of spectrum analysis view feature, the stratigraphic division results are generally good, as shown in Fig. 11(b). First, 2 of the 7 stratigraphic interface points, the 6-*th* and 7-*th* interface points, are completely fitted. Second, the division of other layered points does not deviate substantially from the original interface with maximum deviation under one cycle of the seismic wave. In addition, the stratigraphic labelling is correct. Finally, each stratigraphic interface point is located in the trough of the seismic wave, which closely follows the characteristics and principles of the original stratigraphic division. Among the three training sets, the stratigraphic division of the seismic Gabor feature set has the best results. 4 of 7 interface points that are completely correct, namely the 1-*th*, 2-*th*, 3-*th* and 6-*th* points. For the 5-*th* and 7-*th* division points, only 1 sample point deviates from the original interface position. The difference between the fourth division point and the original division point is within one cycle.

The stratigraphic division profile is projected onto the seismic profile data for analysis of the overall performance of the seismic Gabor feature set. When the seismic amplitude data, spectrum analysis view data, and seismic Gabor features are used as datasets, the division results of section 2222 with the SVM classifier are shown in Figs. 12, 13 and 14, respectively.

To improve the visualization, we identify the locations where the stratigraphic interface has a high amplitude but a poor division result with a red ellipse on the seismic cross-section. The amplitude of the stratigraphic interface is weak, and the areas where the division causes large fluctuations are indicated by red rectangles. For the convenience of description, the 7 automatically divided interfaces are marked with Nos. 1-7. The stratigraphic division results based on the seismic amplitude data are shown in Fig. 13. The 1-*th* (No. 1), 4-*th* (No. 4) and 6-*th* (No. 6) stratigraphic interfaces showed different degrees of fluctuation in the strata with strong amplitudes, high continuity and lateral stability. Especially for the 4-*th* (No. 4) stratigraphic division interface, the division at the middle position fluctuates dramatically, and the difference between some division points and the actual division point is nearly 120 simple points. For stratigraphic interfaces with weak seismic amplitudes, the division results

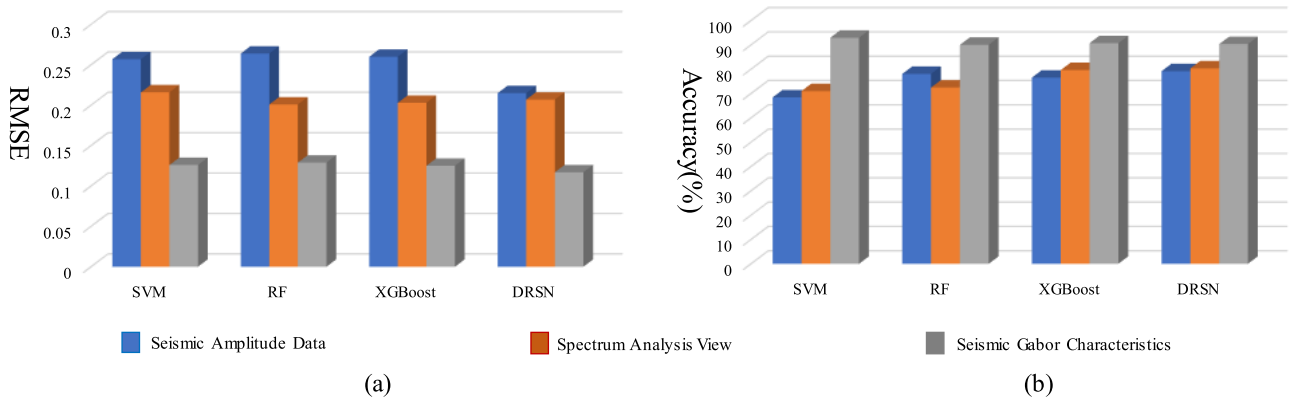

FIGURE 10. RMSE and accuracy of different classifiers using different datasets. (a) shows the RMSE, while (b) shows the accuracy.

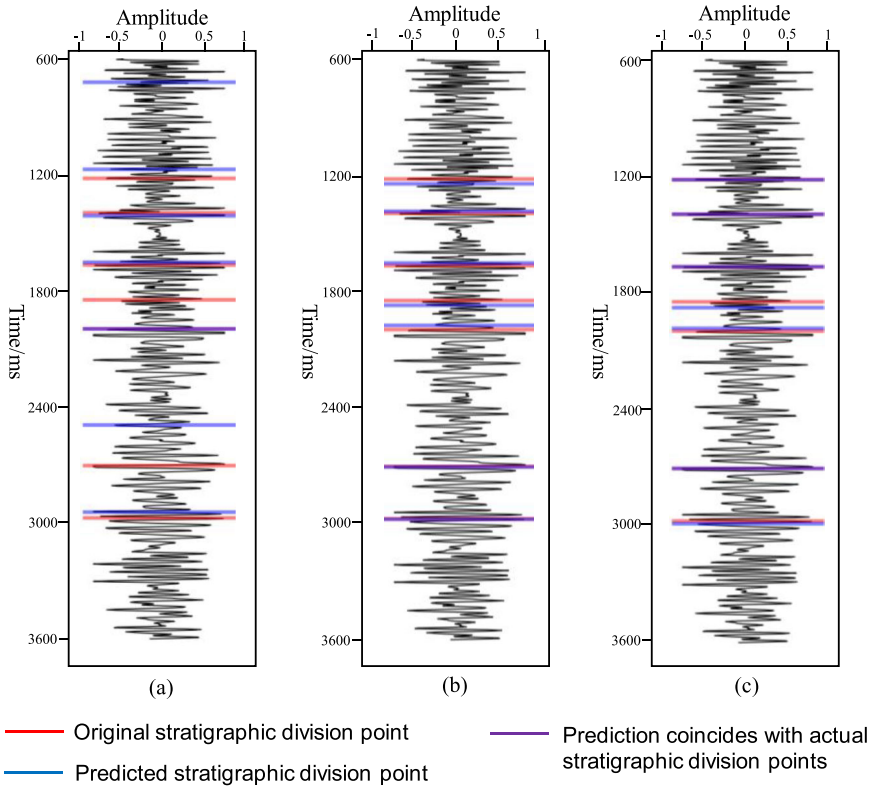

FIGURE 11. Seismic single-trace division results of three datasets with the SVM classifier. The red line is the original division point of the strata. The blue line is the stratigraphic division point of the SVM classifier. The purple line indicates that the original division point of the strata completely coincides with the boundary of the strata divided by the SVM classifier. (a) is the division result of the seismic amplitude dataset. (b) is the division result of the spectrum analysis view. (c) is the division result of the seismic Gabor features.

are more volatile, as shown by the red rectangles in the 6-*th* (No. 6) and 7-*th* (No. 7) interfaces in Fig. 12. Within the red rectangle, both the horizontal and vertical division fluctuations are dramatic. The poor matching is nearly up to 40 seismic traces. In general, the stratigraphic division results based on the seismic amplitude data are not satisfactory.

The stratigraphic division results based on the addition of seismic spectrum analysis view are shown in Fig. 13. Although there are some deviations in the division of the strata with strong seismic amplitudes, high continuity and lateral stability, the deviations are not that dramatic. Moreover, the vertical division fluctuations do not deviate considerably from those at the true division point, and the poor matching range is small, as shown in the 2-*th* (No. 2), the 3-*th* (No. 3), the 4-*th* (No. 4) and the 6-*th* (No. 6) interfaces in Fig. 13 with the red ovals. At locations with weak seismic amplitudes,

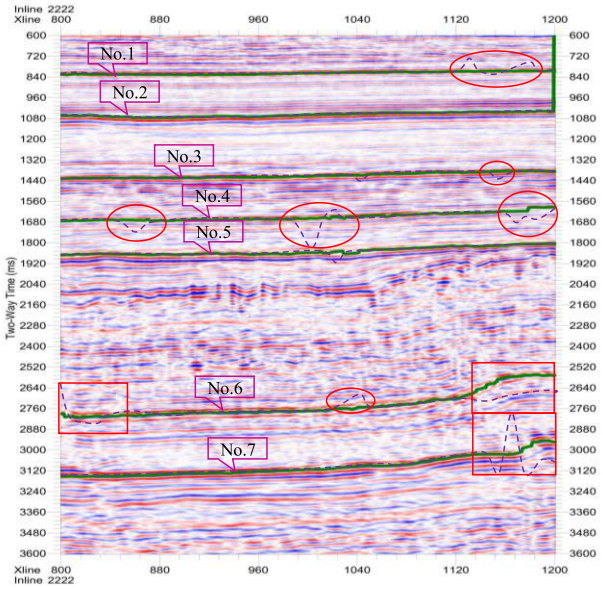

FIGURE 12. Result of stratigraphic division of seismic profile 2222 with the seismic amplitude data.

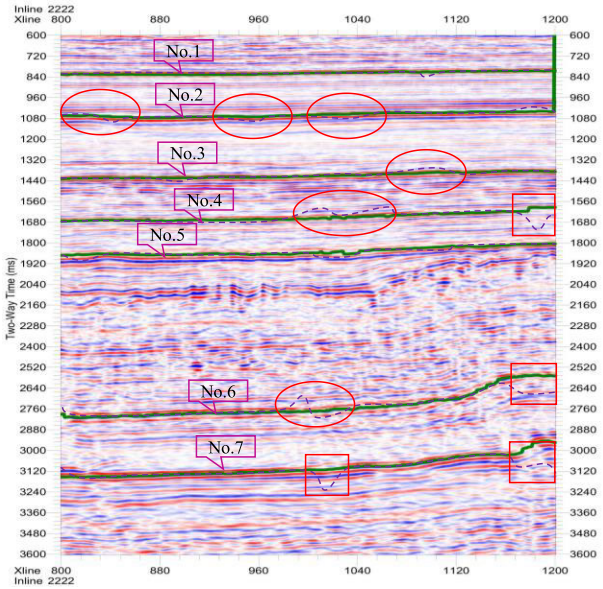

FIGURE 13. Result of stratigraphic division of seismic profile 2222 with the spectral analysis view data.

lateral discontinuities and chaotic seismic wave reflections, the magnitude of fluctuations and the extent of poor match is smaller than those of the division with the seismic amplitude dataset only. These features are indicated with red rectangles in the 4-*th*, 6-*th* and 7-*th* interfaces in Fig. 13. In general, the stratigraphic division results using the addition of seismic spectrum analysis view dataset are within an acceptable range.

The stratigraphic division results based on the addition of seismic Gabor feature dataset are shown in Fig. 14. Lateral fluctuations are small at the divided interface with a strong seismic amplitude, high continuity and good lateral stability. The deviation between the automatically divided interface and the original interface is very small and essentially within 5 sampling points, as shown in Fig. 14 for the 1-*th* (No. 1), 2-*th* (No. 2), 4-*th* (No. 4), 5-*th* (No. 5) and 7-*th* (No. 7) interfaces, which are marked with red ovals. Although the stratigraphic division at locations with weak seismic amplitudes, poor continuity, and poor lateral stability fluctuated in some degrees, the magnitude of the lateral fluctuations and the extent of poor match were much smaller than those of the seismic amplitude dataset and seismic spectrum analysis view dataset. In general, when the seismic Gabor feature dataset is used for stratigraphic division, the overall shape and trend of the divided interface are roughly consistent with those of the original divided interface, satisfying stratigraphic division for practical applications.

Besides conventional machine learning classifiers, we also show the stratigraphic segmentation results based on seismic Gabor features and DRSN, as shown in Fig. 15. For the stratigraphic division in the regions with strong seismic amplitude, high continuity and lateral stability, although there is a deviation, the magnitude of the deviation is small. For example, in the division of the 1-*th,* 2-*th* and 6-*th* layers, the poor match is within 30 traces. In the stratigraphic division of the 3-*th*, 5-*th* and 7-*th* layers, the fluctuation is dramatic, but the amplitude of the fluctuation is small, as shown in the red rectangular area in Fig. 15. For the strata division with weak seismic amplitude, lateral discontinuity and disordered reflected waves, although the mismatch is large, the lateral poor match area is small. Overall, the stratigraphic division results of DRSN are acceptable.

B. SUMMARY OF THE EXPERIMENT

When the strata interface is relatively stable (the seismic event is continuous and the direction changes little) and the amplitude difference between the seismic waves above and below the interface is small, the stratigraphic division results are satisfactory. Where the amplitude difference between the interfaces is small and the seismic event is chaotic, the stratigraphic division points have large mismatch. This occurs because the seismic Gabor feature is mainly based on the energy change in the seismic wave. The insignificant change in the amplitude above and below the stratigraphic interface causes a small energy difference above and below the interface. Thus, the seismic Gabor characteristics are not clear. At the same time, the weaker seismic amplitude leads to a weaker seismic wave energy and a less noticeable energy change. Finally, when the event of the seismic wave is chaotic, energy dispersion occurs in the spectrum analysis view, which is the main reason for the large mismatches of the stratigraphic division point. Although 4 scales and 6 directions are used in the Gabor wavelet transform to extract the seismic Gabor features, the stratigraphic division in locations with weak seismic amplitudes, discontinuities and disordered

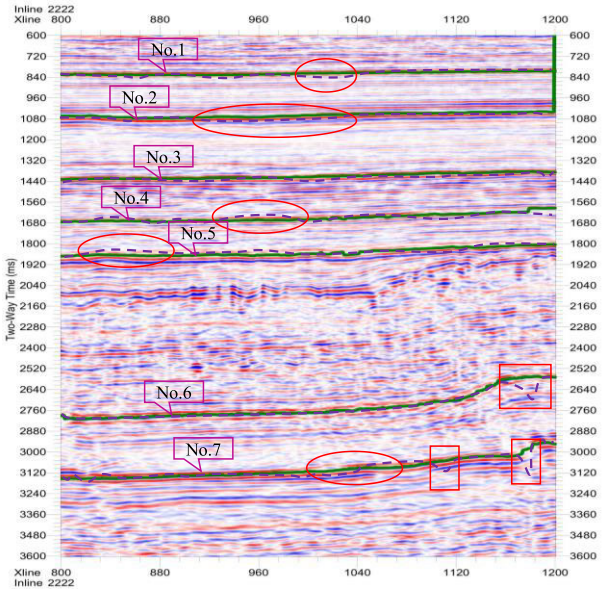

FIGURE 14. Result of stratigraphic division of seismic profile 2222 with the seismic Gabor characteristic data.

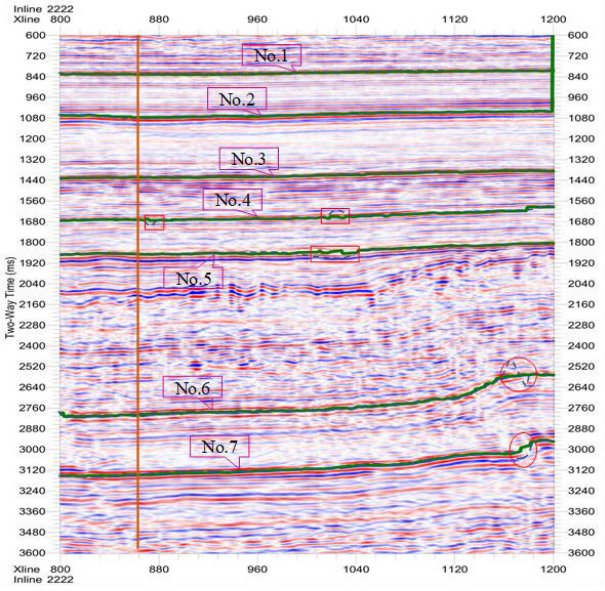

FIGURE 15. Stratigraphic division of No. 2222 based on seismic Gabor features and DRSN classifier.

phase deviates far from the original position. The deviation of the results with the method proposed in this paper is much less than the deviations of the seismic amplitude dataset and seismic spectrum analysis view dataset.

C. PRACTICAL APPLICATION

In the previous experiments, we tested the extracted seismic Gabor features and achieved good results. Finally, we applied this method to actual seismic exploration project. The study area is located in the No. 46 well area of a basin in the southern part of the Tianshan Mountains. The specific location is shown in Fig. 16.

We extracted the amplitude data of a seismic profile passing through the No. 46 key well from a 3D seismic database acquired in the study area, as shown in Fig. 16. The abscissa on the display is the line number, which is marked at the top of the seismic section. Trace 493 in the lower right corner indicates that the seismic trace 493 of each survey line was extracted when the seismic profile was created. The location of well 46 in the seismic profile is marked with a brown straight line. The log profiles from left to right are the natural gamma curve (GR), depth, lithology, sedimentary facies, deep lateral resistivity (RD) and medium lateral resistivity (RM). Among them, the lithology includes the colour of the rock. The strata divided by the lithology, geophysical parameters and geological environment are marked in the well profile. In addition to the above data, the palaeontology and sedimentary evolution characteristics are used as references to have a continuous adjustment, and divided the drilling geological profile into 6 interfaces, which were denoted as Nos.

The specific division of the well profile was based on pattern changes in the GR, RD and RM curves, as well as lithology differences in the lithological columns. For example, in the first interface (No. 1), the GR value suddenly decreases, while the RD and RM values suddenly increase, and the lithology on both sides of the interface also changes greatly. In the seismic profile, the seismic waves have a strongly reflection, laterally continuous and stable. There are no issues with the division of the first interface. In the second interface (No. 2), the No. 46 well position and the positions on both sides of the well have strong reflections, good lateral continuity and good stability, and the stratigraphic division is accurate. In the few locations away from the well where the seismic wave reflection is weak, the stratigraphic division has large fluctuations, however, the lateral range of the fluctuations is small, as shown by the green rectangle in Fig. 17. The third (No. 3) interface is similar to the first interface, and the automatic stratigraphic division result is very accurate. Most of the strata in the 4-*th* (No. 4) and 5-*th* (No. 5) interfaces have strong reflection, good continuity and lateral stability, and division the strata is reliable. However, in the last part of the 4-*th* and 5-*th* layer interfaces, the seismic reflections are weak and disordered. Although there are no major fluctuations in the stratigraphic division, according to the experimental results, the reliability of the stratigraphic division is low for similar cases, which is marked by the red rectangle on the 4-*th* and 5-*th* interfaces in Fig. 17. In the 6-*th* (No. 6) interface, the seismic wave reflection is weak for the entire interface, and the continuity and lateral stability are poor. The division result has large fluctuations and low reliability, as indicated by the red ellipse in the No. 7 formation interface in Fig. 17. In the well geological profile that corresponds to this interface, the changes in the GR, RD and RM curves at the interface are not clear, and the lithology varies. Manual classification based on log data is also difficult. Thus, we must combine lithofacies paleogeography, sedimentary

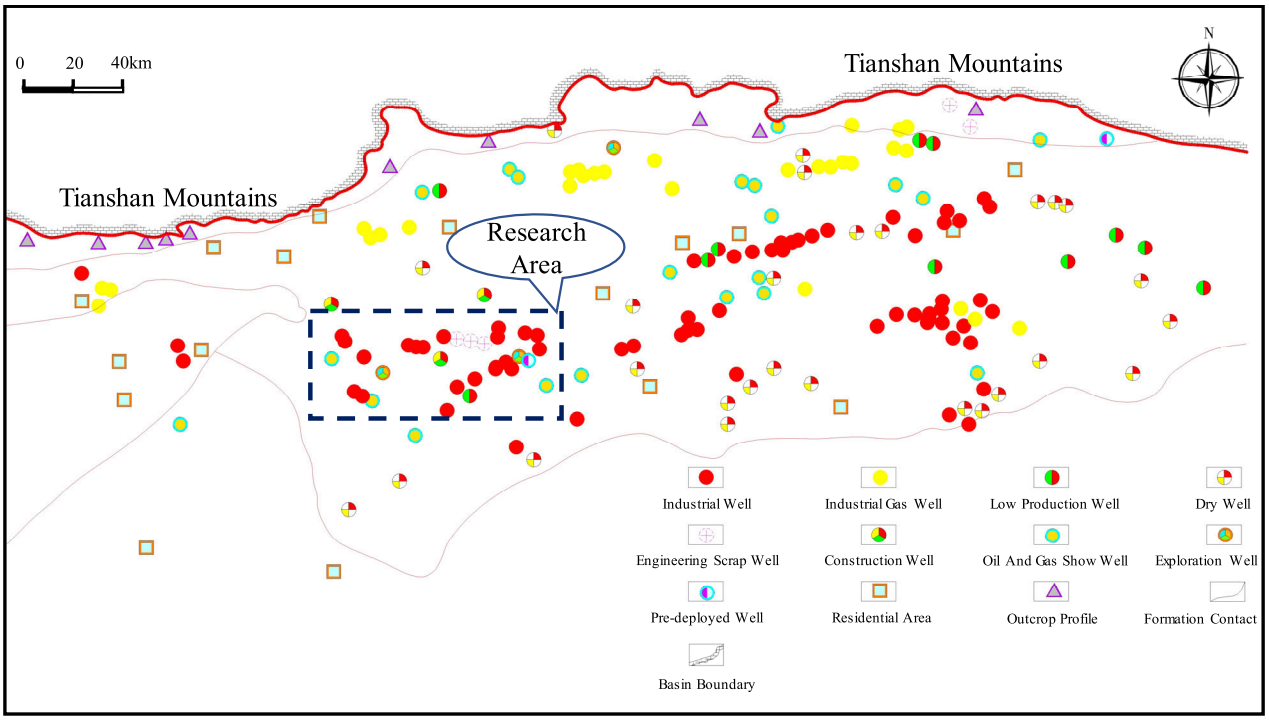

FIGURE 16. The scope of the study area and the distribution map of well locations. The map marks the specific conditions of drilling work in the study area and surrounding areas, including industrial oil and gas wells, low production wells, and dry wells.

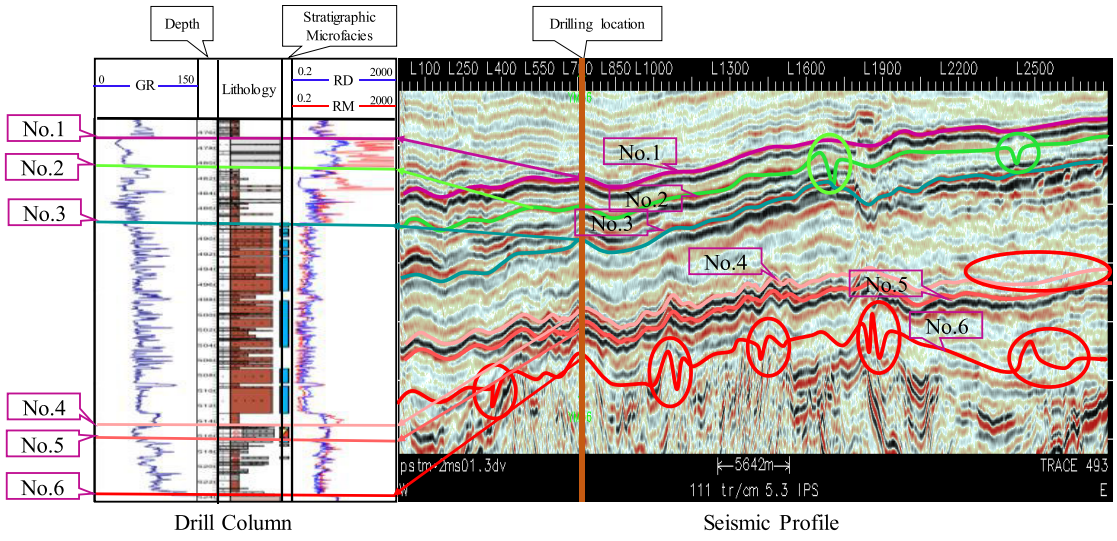

FIGURE 17. Practical application of seismic Gabor feature horizon division.

environment and other data with the adjacent well data to complete the division of the strata.

V. CONCLUSION

In this paper, a seismic attribute feature extraction method based on the Gabor wavelet transform is proposed. Unlike traditional methods for the extraction of seismic amplitude features, this method fully uses the time domain, frequency domain and energy information of the seismic signals to ensure that the extracted feature can be more repositioning the formation changes. To verify the effectiveness of the method, in this paper, seismic amplitude data, spectrum analysis view data and extracted seismic Gabor features are used as training sets, and the SVM, RF, XGBoost and DRSN algorithms are used to verify the extracted features. The verification results show that the extracted seismic Gabor features are better than traditional features such as waveforms. Finally, we applied this method in practice. In the practical application,

we compared the automatic stratigraphic division results with well geological profiles. The comparison results show that the seismic signal data can be converted into a spectrum analysis view dataset and that the Gabor wavelet transform can be used to extract data features. The method and process of converting the seismic signals into geological features in the practical ways.

REFERENCES

[1] K. Xu and Y. Li, "Integrated interpretation of gravity, magnetic, seismic, and well data to image volcanic units for oil-gas exploration in the eastern Junggar Basin, Northwest China," *Interpretation*, vol. 8, no. 4, pp. SS113–SS127, Nov. 2020, doi: 10.1190/int-2019-0280.1.

[2] H. Zeng, X. Zhu, R. Zhu, and Q. Zhang, "Seismic prediction of sandstone diagenetic facies: Applied to cretaceous Qingshankou formation in Qijia depression, Songliao Basin, East China," *Petroleum Exploration Develop.*, vol. 40, no. 3, pp. 287–295, Jun. 2013, doi: 10.1016/s1876-3804(13)60035-x.

[3] S. Wei, M. V. DeAngelo, and B. A. Hardage, "Advantages of joint interpretation of P–P and P–SV seismic data in geothermal exploration," *Interpretation*, vol. 2, no. 2, pp. SE117–SE123, May 2014, doi: 10.1190/int-2013-0084.1.

[4] P. Wang, X. Chen, B. Wang, J. Li, and H. Dai, "An improved method for lithology identification based on a hidden Markov model and random forests," *Geophysics*, vol. 85, no. 6, pp. IM27–IM36, Nov. 2020, doi: 10.1190/geo2020-0108.1.

[5] L.-P. Sun, X.-D. Zheng, H. Shou, J.-S. Li, and Y.-D. Li, "Quantitative prediction of channel sand bodies based on seismic peak attributes in the frequency domain and its application," *Appl. Geophys.*, vol. 7, no. 1, pp. 10–17, Mar. 2010, doi: 10.1007/s11770-010-0009-y.

[6] Q. Rong and X. Qiao, "FBG for oil and gas exploration," *J. Lightw. Technol.*, vol. 37, no. 11, pp. 2502–2515, Jun. 13, 2019, doi: 10.1109/JLT.2018.2866326.

[7] D. Park and T. Kishida, "Shear wave velocity profiles of fill dams," *Soil Dyn. Earthq. Eng.*, vol. 104, pp. 250–258, Jan. 2018, doi: 10.1016/j.soildyn.2017.10.013.

[8] J. Deeks and D. Lumley, "Prism waves in seafloor canyons and their effects on seismic imaging," *Geophysics*, vol. 80, no. 6, pp. S213–S222, Nov. 2015, doi: 10.1190/geo2015-0014.1.

[9] D. Anache-Ménier, B. A. van Tiggelen, and L. Margerin, "Phase statistics of seismic coda waves," *Phys. Rev. Lett.*, vol. 102, no. 24, pp. 1–11, Jun. 2009.

[10] L. Li, Q. Lyu, and F. Shang, "Seismic prediction of lithofacies heterogeneity in Paleogene Hetaoyuan shale play, Biyang depression, China," *Open Geosci.*, vol. 12, no. 1, pp. 1383–1391, Nov. 2020, doi: 10.1515/geo-2020-0202.

[11] Q. Luo, Y. Wang, Y. Zheng, X. Chang, B. Wang, and R. Zeng, "High-dimensional co-occurrence matrix: A new tool for 3D seismic target visualization and interpretation," *Interpretation*, vol. 8, no. 4, pp. T967–T979, Nov. 2020, doi: 10.1190/int-2019-0127.1.

[12] M. Zhonghua, "Seismic data attribute extraction based on Hadoop platform," in *Proc. IEEE 2nd Int. Conf. Cloud Comput. Big Data Anal. (ICCCBDA)*, Apr. 2017, pp. 180–184.

[13] J. Zheng, G. Zhu, and M. Liu, "Vibrator data denoising based on fractional wavelet transform," *Acta Geophysica*, vol. 63, no. 3, pp. 776–788, Jun. 2015, doi: 10.1515/acgeo-2015-0009.

[14] Y. Tian, Y. Li, H. Lin, and H. Ma, "A sparse NMF-SU for seismic random noise attenuation," *IEEE Geosci. Remote Sens. Lett.*, vol. 10, no. 3, pp. 607–611, May 2013, doi: 10.1109/LGRS.2012.2215835.

[15] T. Zhang, G. Feng, J. Liang, and T. An, "Acoustic scene classification based on mel spectrogram decomposition and model merging," *Appl. Acoust.*, vol. 182, Nov. 2021, Art. no. 108258, doi: 10.1016/j.apacoust.2021.108258.

[16] C. S. Qian, D. Z. Liu, Z. G. Liu, and X. H. Li, "EMD based on recursive high-pass filter and its application on seismic signal analysis," *Chin. J. Geophys.*, vol. 53, no. 5, pp. 1215–1225, May 2010, doi: 10.3969/j.issn.0001-5733.2010.05.024.

[17] R. Babić, L. Babić, and B. Jakšić, "New aspect of transition between line and continuous spectrum and its relation to seismic influence on structures," *Scientia Iranica*, vol. 27, no. 3, pp. 1515–1524, Apr. 2018, doi: 10.24200/sci.2018.20326.

[18] Y. Zhao, X. Luo, X. Lin, H. Wang, X. Kui, F. Zhou, J. Wang, Y. Chen, and W. Chen, "Visual analytics for electromagnetic situation awareness in radio monitoring and management," *IEEE Trans. Vis. Comput. Graphics*, vol. 26, no. 1, pp. 590–600, Jan. 2020, doi: 10.1109/TVCG.2019.2934655.

[19] L. Guo, R. Luo, X. Li, Y. Zhou, T. Juanjuan, and C. Lei, "Seismic random noise removal based on a multiscale convolution and densely connected network for noise level evaluation," *IEEE Access*, vol. 10, pp. 13911–13925, 2022.

[20] L. Guo, L. Renze, L. Xingyu, T. Juanjuan, C. Lei, and Z. Yang, "Logging data completion based on an MC-GAN-BiLSTM model," *IEEE Access*, vol. 10, pp. 1810–1822, 2022, doi: 10.1109/ACCESS.2021.3138194.

[21] R. Luo, L. Guo, X. Li, J. Tuo, C. Lei, and Y. Zhou, "An eXtreme gradient boosting algorithm combining artificial bee colony parameters optimized technique for single sand body identification," *IEEE Access*, vol. 9, pp. 156894–156906, 2021, doi: 10.1109/ACCESS.2021.3129830.

[22] L. Navarro, G. Courbebaisse, and J.-C. Pinoli, "Continuous frequency and phase spectrograms: A study of their 2D and 3D capabilities and application to musical signal analysis," *J. Zhejiang Univ. Sci. A*, vol. 9, no. 2, pp. 199–206, Feb. 2008, doi: 10.1631/jzus.a072140.

[23] S. Zu, H. Zhang, and Z. Duan, "Singing voice separation by low-rank and sparse spectrogram decomposition with prelearned dictionaries," *J. Audio Eng. Soc.*, vol. 65, no. 5, pp. 377–388, May 2017, doi: 10.17743/jaes.2017.0009.

[24] J. Wang, L. Yan, Q. Yang, and M. Yuan, "Speech enhancement based on perceptually motivated guided spectrogram filtering," *J. Intell. Fuzzy Syst.*, vol. 40, no. 3, pp. 5443–5454, Mar. 2021, doi: 10.3233/jifs-202278.

[25] W. Yang, X. Gong, and W. Li, "Geological origins of seismic bright spot reflections in the Ordovician Strata in the Halahatang area of the Tarim basin, Western China," *Can. J. Earth Sci.*, vol. 55, no. 12, pp. 1297–1311, Dec. 2018, doi: 10.1139/cjes-2018-0055.

[26] H. Zeng, W. Wang, and Q. Liang, "Seismic expression of delta to deep-lake transition and its control on lithology, total organic content, brittleness, and shale-gas sweet spots in Triassic Yanchang formation, southern Ordos basin, China," *Interpretation*, vol. 5, no. 2, pp. SF1–SF14, May 2017, doi: 10.1190/int-2016-0095.1.

[27] H. Tao, R. Liang, C. Zha, X. Zhang, and L. Zhao, "Spectral features based on local Hu moments of Gabor spectrograms for speech emotion recognition," *IEICE Trans. Inf. Syst.*, vol. 99, no. 8, pp. 2186–2189, 2016, doi: 10.1587/transinf.2015EDL8258.

[28] B. Kubicek, A. Sen Gupta, and I. Kirsteins, "Sonar target representation using two-dimensional Gabor wavelet features," *J. Acoust. Soc. Amer.*, vol. 148, no. 4, pp. 2061–2072, Oct. 2020, doi: 10.1121/10.0002168.

[29] W. Zheng and H. Deng, "High-resolution sequence stratigraphic division and distribution of tidal deposits in the Zhuhai formation, Huizhou Sag, Pearl River Mouth basin, South China Sea," *Geolog. Mag.*, vol. 149, no. 4, pp. 722–728, Jul. 2012, doi: 10.1017/s0016756811000768.

[30] L. Chen, Y. Lu, T. Guo, F. Xing, and Y. Jiao, "Seismic sedimentology study in the high-resolution sequence framework—A case study of platform margin Reef-beach system of Changxing formation, Upper Permian, Yuanba area, Northeast Sichuan basin, China," *J. Earth Sci.*, vol. 23, no. 4, pp. 612–626, Aug. 2012, doi: 10.1007/s12583-012-0278-x.

[31] S. T. Thota, M. A. Islam, and M. R. Shalaby, "A 3D geological model of a structurally complex relationships of sedimentary facies and petrophysical parameters for the late miocene Mount messenger formation in the Kaimiro–Ngatoro field, Taranaki basin, New Zealand," *J. Petroleum Exploration Prod. Technol.*, vol. 12, no. 4, pp. 1147–1182, Apr. 2022, doi: 10.1007/s13202-021-01366-0.

[32] J. Yao, P. Krolak, and C. Steele, "The generalized Gabor transform," *IEEE Trans. Image Process.*, vol. 4, no. 7, pp. 978–988, Jul. 1995, doi: 10.1109/83.392338.

[33] D. M. Onchis, "Signal reconstruction in multi-windows spline-spaces using the dual system," *IEEE Signal Process. Lett.*, vol. 19, no. 11, pp. 729–732, Nov. 2012, doi: 10.1109/LSP.2012.2213591.

[34] D. M. Onchis and S. Zappalà, "Approximate duals of Gabor-like frames based on realizable multi-window spline-type constructions," in *Proc. 18th Int. Symp. Symbolic Numeric Algorithms Sci. Comput. (SYNASC)*, Timisoara, Romania, Sep. 2016, pp. 99–104, doi: 10.1109/SYNASC.2016.027.

[35] A. T. Catherall and D. P. Williams, "High resolution spectrograms using a component optimized short-term fractional Fourier transform," *Signal Process.*, vol. 90, no. 5, pp. 1591–1596, May 2010, doi: 10.1016/j.sigpro.2009.11.004.

[36] J. R. Rausch and K. Kelley, "A comparison of linear and mixture models for discriminant analysis under nonnormality," *Behav. Res. Methods*, vol. 41, no. 1, pp. 85–98, Feb. 2009, doi: 10.3758/brm.41.1.85.
[37] D. Chu, L.-Z. Liao, M. K. P. Ng, and X. Wang, "Incremental linear discriminant analysis: A fast algorithm and comparisons," *IEEE Trans. Neural Netw. Learn. Syst.*, vol. 26, no. 11, pp. 2716–2735, Nov. 2015, doi: 10.1109/TNNLS.2015.2391201.

RAN XIONG was born in Tianmen, Hubei, China, in 1983. He received the master's degree from the Yangtze University of Geosciences, China, in 2009. He is currently with the Petrochina Hangzhou Research Institute of Geology and he has been engaged in comprehensive research on carbonate rock and oil geology for a long time.

XURI HUANG was born in Guilin, Guangxi, China, in 1965. He received the Ph.D. degree from the University of Tulsa, in 1995. He is currently with Southwest Petroleum University and he has been researched on data fusion of reservoir geophysics and reservoir oriented imaging methods.

LIANG GUO was born in Xiantao, Hubei, China, in 1983. He received the master's degree from the Kunming University of Science and Technology, China, in 2018. He is currently pursuing the Ph.D. degree with Southwest Petroleum University. He is mainly engaged in the work of exploration geophysics and big data processing deep learning. He is employed at the Sichuan College of Architectural Technology Department of Railway Engineering, engaging in research and teaching related to artificial intelligence methods in seismic exploration.

XUAN ZOU was born in Jingmen, Hubei, China, in 1988. He received the bachelor's degree from the China University of Geosciences, Wuhan, in 2011. He is currently the Project Manager of the Central South Geological Survey Institute of China Metallurgical Geology Burea. He is mainly engaged in geology, mineral resources, and exploration geophysics.

HAONAN TIAN was born in Xiangcheng, Henan, China, in 1989. He received the master's degree from the China University of Petroleum, Beijing, in 2015. He is mainly engaged in the work of seismic interpretation and reservoir prediction.